

Laser-Splashed Plasmonic Nanocrater for Ratiometric Upconversion Regulation and Encryption

Ziwei Feng, Dejiao Hu, Liangliang Liang, Jian Xu, Yaoyu Cao, Qiuqiang Zhan, Bai-Ou Guan, Xiaogang Liu,* and Xiangping Li*

Upconversion nanoparticles (UCNPs) with exceptional optical properties have emerged as a new paradigm for data encryption through multicolor coding, lifetime tuning, and excitation light phasing. However, in addition to low internal quantum efficiency, the utility of UCNPs for data encryption is largely hampered by the requirement of multiple sets of UCNPs of complex compositions with specifically tailored optical properties. Herein, it is found that metal–insulator–metal (MIM) configurations are capable of regulating upconversion emission of UCNPs through programmable geometry-dependent plasmonic features of laser-splashed submicron cavities. Furthermore, a ratiometric encryption strategy by regulating the ratio of dual-band emission of a single set of UCNPs of fixed composition placed within the plasmonic MIM configuration is demonstrated. High-throughput encryption and decryption through the luminescence ratiometric strategy can be achieved in a facile laser writing fashion with upscalability and sub-micrometer-scale precision. This demonstration opens a new route to luminescence modulation with large encoding capacity and underpins potential applications of UCNPs in multiplexed data storage and information encryption.

Optical multiplexing and encoding based on light–matter interactions in physical dimensions such as polarization,^[1–3] wavelength,^[4–6] angular dispersion,^[7–9] and orbital angular momentum^[10–12] have been well heralded as an enabling platform for high-security encryption applications in banknotes, ID cards, and so on.^[13,14] Among these well-developed optical

encoding strategies, spectral encryption based on spatial patterning of luminescent materials possessing distinct emission features is widely implemented.^[15–17] With innate virtues such as superior photostability, narrow emission bandwidths, and long luminescence lifetime, lanthanide-doped upconversion nanoparticles (UCNPs) have been extensively applied in many emerging areas such as 3D displays,^[18,19] biomedical imaging,^[20–22] solar cells,^[23–25] lasing,^[26,27] and especially data encryption.^[28–30] Notably, the high designability in emission bands, strong resistance to photobleaching, and low autofluorescence interference make UCNPs a promising alternative to conventional fluorophores (such as organic dyes and quantum dots) in high-capacity and long-term optical encoding applications.^[31–33] Over the past few years, UCNP-mediated data encryption through multicolor barcoding,^[6] lifetime

tuning,^[34–36] and phase angle hybridization^[37] has been successfully demonstrated. Nevertheless, these encoding strategies rely on a different set of UCNPs to achieve distinct emission features in confined temporal or spatial regions, which would inevitably introduce the difficulty to the design of data multiplexing and sample synthesis.

Plasmonic nanomaterials, working as optical antennas, can enormously intensify their adjacent local fields to tailor light–matter interactions on demand through tuning the geometry, equilibrium configuration, or choice of nanoantenna materials.^[38] Especially those noble metal nanostructures (such as Au and Ag) featuring surface plasmon resonances, have proven effective in tuning the emission properties of UCNPs. By varying the size or aspect ratio of these plasmonic nanostructures, their resonance bands can be precisely tuned to match either the absorption or emission bands of adjacent UCNPs. Therefore, the excitation rate or radiative emission rate of UCNPs could be programmably enlarged to achieve luminescence enhancement for the whole spectrum or any specific emission band.^[39–48] The integration of plasmonic nanostructures with UCNPs opens new encoding strategies in addition to enhanced upconversion luminescence (UCL) intensities.^[49,50] However, the inherent high electrical conductivity of metallic materials can suppress the quantum yields of emission when the UCNPs are in contact with the metallic surface.^[51,52]

Z. Feng, Dr. D. Hu, J. Xu, Prof. Y. Cao, Prof. B.-O. Guan, Prof. X. Li
Guangdong Provincial Key Laboratory of Optical Fiber Sensing
and Communications

Institute of Photonics Technology
Jinan University
Guangzhou 511443, P. R. China
E-mail: xiangpingli@jnu.edu.cn

Dr. L. Liang, Prof. X. Liu
Department of Chemistry
National University of Singapore
Singapore 117543, Singapore
E-mail: chmlx@nus.edu.sg

Prof. Q. Zhan
Centre for Optical and Electromagnetic Research
South China Academy of Advanced Optoelectronics
South China Normal University
Guangzhou 510006, P. R. China

 The ORCID identification number(s) for the author(s) of this article can be found under <https://doi.org/10.1002/adom.201900610>.

DOI: 10.1002/adom.201900610

Consequently, the maximum enhancement in upconversion luminescence can only be achieved at a moderate distance (≈ 10 nm) separating the nanoparticle and the metal surface. Despite recent studies on plasmonic coupled upconversion luminescence with large enhancement and precise color tuning, plasmonic spacing control and high-precision fabrication through complicated treatments and time-consuming lithography techniques remain daunting challenges.

Herein, we report programmable plasmonic couplers based on a metal–insulator–metal (MIM) configuration for upconversion luminescence regulation and high-throughput ratiometric encryption. In a typical experiment, Ti-Si₃N₄-Ag MIM structure was first fabricated, and plasmonic nanocraters with different splashing morphologies on the MIM substrate were reproducibly printed upon irradiation of a single femtosecond pulse laser. The resonances of the nanocraters could be exquisitely designed through controlling their morphologies via laser dose tuning. In our study, two types of nanocraters with resonance frequencies in coincidence with green (538 nm) and red (644 nm) emission bands of NaYF₄:Yb/Ho/Ce UCNPs were fabricated. The selective wavelength coupling led to distinct luminescence enhancement in the two emission bands, allowing laser-printed images to be encoded at sub-micrometer levels with ratiometric luminescence.

The concept of plasmonic nanocrater modulated dual upconversion emission is illustrated in **Figure 1**. The nanocrater pattern was printed onto a MIM three-layer configuration using a femtosecond pulsed laser (40 fs at 800 nm). Through tuning the morphologies and thus the resonance frequencies of fabricated nanocraters via pulse dose controlling, the ratiometric luminescence (red and green) of the UCNPs dispersed onto the pattern can be precisely controlled. Through this approach, we demonstrated high-throughput information encryption using a single set of UCNPs in a lithography-free fashion. The MIM configuration is adopted to boost the laser printing effects by quickly building up the localized fields while providing a cavity for forming Fabry–Perot resonances. Since the silver film can have the largest reflection in the visible region, a silver film of about 135 nm thickness was chosen as the grounding layer. As titanium has a small extinction coefficient and the thin oxide

layer (2–3 nm) formed on its surface natively prevents the degradation, the cladding layer was set as a titanium film of 40 nm thickness. The spacer layer is made of silicon nitride (Si₃N₄), which is highly transparent in the visible range and beneficial in manipulating the transient photothermal effects. Core–shell UCNPs consisting of NaYF₄:Yb/Ho/Ce exhibiting a red/green (R/G) ratio of around 3.5 on the cover glass are used here as the upconversion agents (Figure 1b). Two types of nanocrater morphologies were chosen to regulate the emission intensity ratio of the two bands. A nanocrater A with a shallow depth that mainly scatters the Fabry–Perot resonant wavelength was used to enhance the green component. The nanocrater C with a deep depth resonating in the longer wavelength region was utilized to magnify the red emission. As a result, the two types of nanostructures regulate R/G ratios of around 1.8 and 5.5, respectively (Figure 1b).

Upon illumination of femtosecond pulsed laser beams, the titanium film within the focal spot absorbs the energy and gains a momentum perpendicular to the surface in a duration of several picoseconds. Subsequently, the film splashes outward and undergoes fast recrystallization due to the rapid heat dissipation to the surroundings.^[9] Considerably large laser dose (270 mJ cm⁻²) could lead to direct ablation of the titanium film within the focal spot, forming a single nanocrater structure (crater A). A further increase of the pulse energy (461 mJ cm⁻²), the silicon nitride film will also be heated up and ablated, generating a deeper nanocrater (crater B). When keeping increasing pulse dose (1998 mJ cm⁻²), the silver film will also be ablated, generating an additional nanocrater with a smaller radius in the middle layer. Thus, nanostructures consisting of three nanocraters (crater C) can be printed. Consequently, the printing of nanocraters with variant morphologies featuring different resonant frequencies becomes possible through precisely controlling the laser energy density (**Figure 2a**). It indicates that a full-range visible light can be controlled by adjusting different laser parameters. The nanocraters A and C exhibiting major resonance peaks centered at 538 and 650 nm, respectively, are shown in Figure 2b,c. The inset shows the scanning electron microscopy (SEM) images of printed nanocraters with representative morphologies

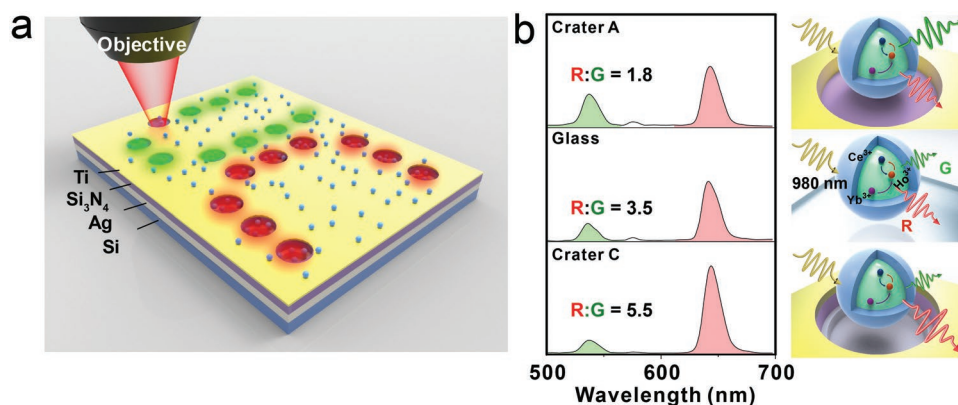


Figure 1. a) The sketch of nanocrater regulated ratiometric upconversion emission. The MIM structure is composed of silver, Si₃N₄, and titanium layer of 135, 169, and 40 nm thickness, respectively. Two types of nanocraters are fabricated by varying the pulse energy. b) The nanocrater A mainly enhances the green emission of UCNPs, while the nanocrater C magnifies the red emission band. The right panel illustrates the composition of UCNPs and UCNPs deposited on different substrates.

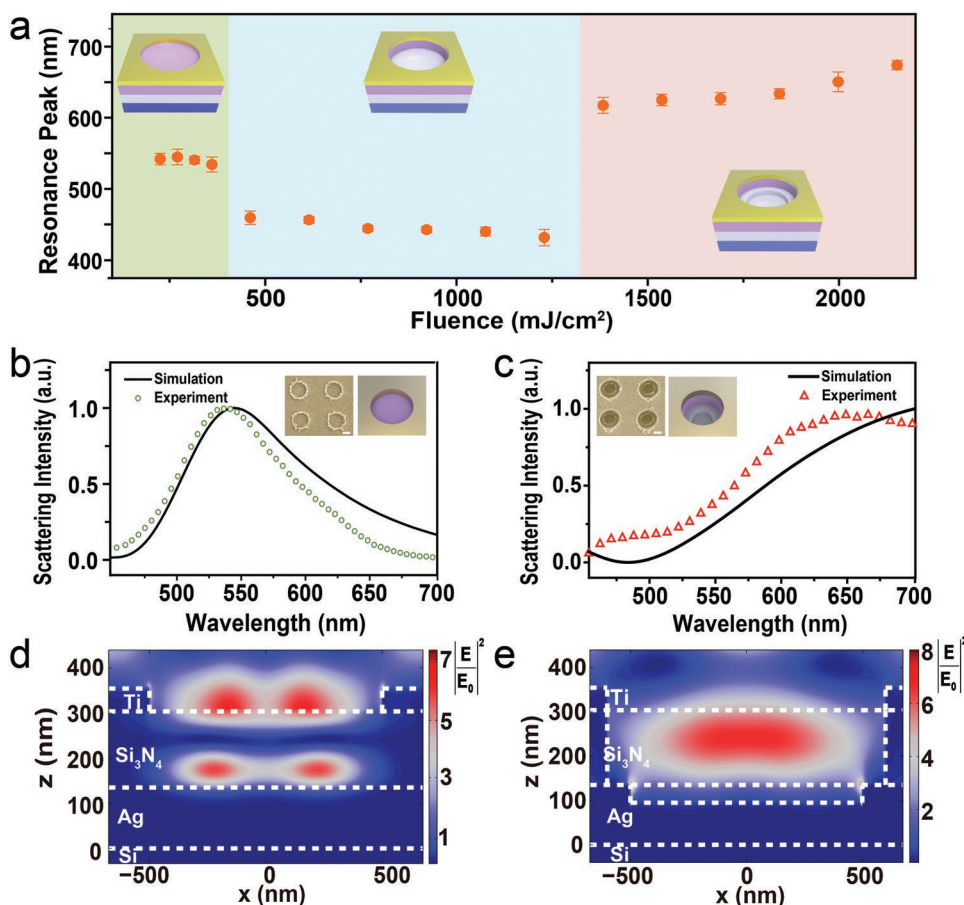


Figure 2. Simulation of field enhancements by nanocraters of different morphologies. a) Resonance peaks of the nanocraters as a function of the laser energy, revealing three regions of resonance frequencies. b,c) Experimental and theoretical plasmonic resonance regions of nanocraters fabricated at 270 and 1998 mJ cm^{-2} , respectively. Insets: Corresponding SEM images of nanocraters. Scale bar: 500 nm. d,e) Simulated electric field distributions upon illumination at 538 and 644 nm, respectively.

(more morphologies of nanocraters are shown in Figure S1, Supporting Information). The peak at 538 nm corresponds to the Fabry–Perot resonance mode in the nanocrater A, and the peak at 650 nm arises from the integrate resonance of the nanocrater C. Experimental measurements are reasonably consistent with simulations (Figure 2b,c). In addition, finite-difference time-domain (FDTD) simulations reveal the electric field distributions in the vicinity of the nanocraters with peak intensity enhancements by seven and eightfolds for green and red emissions, respectively (Figure 2d,e). Meanwhile, the moderate electric field distributions of crater A upon illumination at 644 nm and crater C upon illumination at 538 nm are shown in Figure S2 (Supporting Information). The resonances are in the form of longitudinal gap plasmons in the silicon nitride to promote strong light emissions and can be tuned to match emission bands of UCNP by varying the dosed energy density of fs pulsed beams, which is critical for plasmon coupling with light to achieve optimal field confinements. By removing the luminescence quenching effect of UCNP near the surface of metal nanostructures,^[51] the MIM configuration allows augmented electric fields confined inside nanocraters for efficient luminescence enhancement (Figure S3, Supporting Information).

Figure 3a shows the transmission electron microscopy (TEM) image of the as-prepared $\text{NaYF}_4:\text{Yb}/\text{Ho}/\text{Ce}$ core–shell UCNP. Upon irradiation at 980 nm with a continuous-wave (CW) laser, these UCNP exhibit strong upconversion emission in the visible range with two peaks at 538 and 644 nm, corresponding to the $^5\text{F}_4, ^5\text{S}_2 \rightarrow ^5\text{I}_8$ and $^5\text{F}_5 \rightarrow ^5\text{I}_8$ transition of Ho^{3+} , respectively (Figure 3b). The underlying upconversion transition is illustrated in Figure S4 (Supporting Information). The incident light at the wavelength of 980 nm is absorbed by Yb^{3+} ions through the transition of the $^2\text{F}_{7/2} \rightarrow ^2\text{F}_{5/2}$ with a subsequent step of energy transfer to multiple energy levels in the Ho^{3+} ions.^[18] After certain nonradiative relaxation, upconversion emissions occur in the visible range. The cross-relaxation represents the energy transfer between the Ho^{3+} ions and Ce^{3+} ions.

The as-prepared UCNP were dispersed onto the plasmonic nanocraters through spin-coating (Figure 3c). The UCNP were premixed with a 3 wt% polymethyl methacrylate (PMMA) solution to improve the adhesion to the nanocraters. Figure 3d,e shows that the nanocraters serve as templates to immobilize the UCNP through self-assembly. The upconversion emission from the sample was then collected by using a confocal imaging system where a 980 nm laser was employed as the excitation source (Figure S5, Supporting Information). The acquired

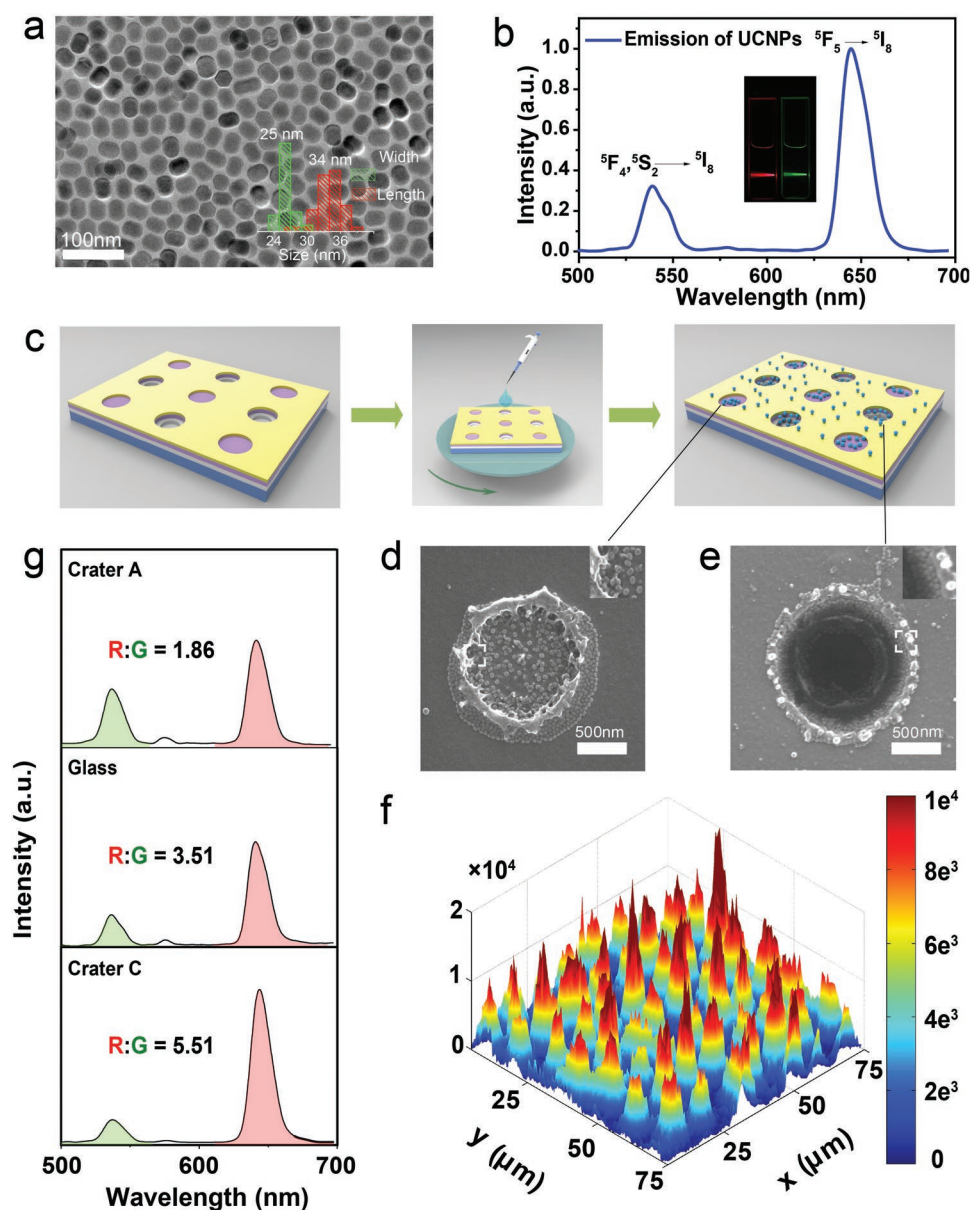


Figure 3. a) TEM image of as-synthesized NaYF₄:Yb/Ho/Ce (20/2/8%) core-shell UCNP nanocraters. Inset: the corresponding size distributions of the UCNP nanocraters. b) Upconversion emission spectrum of the core-shell UCNP nanocraters under a 980 nm CW laser excitation (10 W cm⁻²). Inset: Corresponding luminescence photographs of UCNP nanocraters dispersed in cyclohexane (540 and 655 nm bandpass filter were used before the camera). c) Schematic of spin-coating UCNP nanocraters onto the fabricated nanocraters. d, e) SEM images of nanocraters coated with UCNP nanocraters. f) The confocal image of UCNP nanocraters deposited on nanocrater A. g) Upconversion luminescence spectra from UCNP nanocraters deposited on nanocrater A, glass, and nanocrater C.

intensity profile of the UCNP nanocraters on the nanocrater A is shown in Figure 3f. It is revealed that the upconversion emissions are concentrated around the nanocraters. Figure 3g depicts the emission spectra from the UCNP nanocraters deposited on the glass substrate and two different nanocrater substrates. The ratio of peak intensities between emission wavelengths of 644 nm (R) and 538 nm (G) is 3.51 when the UCNP nanocraters (NaYF₄:Yb/Ho/Ce) are deposited on the glass substrate. However, when the UCNP nanocraters are deposited on a template containing shallow single nanocraters (crater A), the emission at 538 nm is enhanced, resulting in a decreased R/G ratio to 1.86. On the contrary, when the UCNP nanocraters are deposited on a template containing three

nanocraters (crater C), the red band emissions are enhanced, leading to an increased R/G ratio of 5.51. Notably, as shown in Figure S6 (Supporting Information), the ratiometric emission modulation is robust and hardly changes with variations in the UCNP concentration. The UCL spectra of the UCNP nanocraters on (i) the nanocrater A, (ii) the glass, and (iii) the nanocrater C are shown in Figure S7a (Supporting Information) at a saturation excitation power of 1.5×10^5 W cm⁻². Compared to the sample on the glass substrate (the reference), the nanocrater structures exhibit 1.98- and 1.51-fold UCL enhancement factors (EFs) for green and red emissions, respectively, upon high power excitation. Under a weak excitation, an even larger enhancement factor is expected.

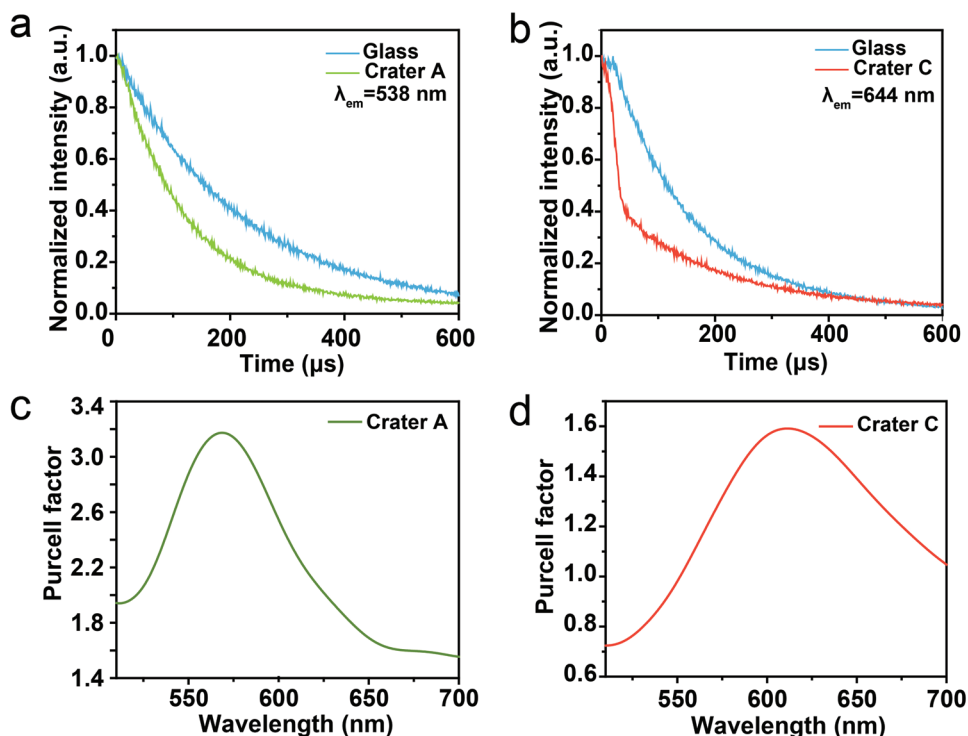


Figure 4. a) Time-resolved photoluminescence (TRPL) of NaYF₄:Yb/Ho/Ce UCNPs deposited on nanocrater A (green) and glass (blue) acquired at the emission wavelength of 538 nm. b) Time-resolved photoluminescence (TRPL) of NaYF₄:Yb/Ho/Ce UCNPs deposited on the nanocrater C (red) and glass (blue). The measurements were acquired at the emission wavelength of 644 nm. c,d) Simulated Purcell factor of UCNPs deposited on the nanocrater A and nanocrater C.

The green and red emission peaks corresponding to the energy transitions of ⁵F₄,⁵S₂→⁵I₈ and ⁵F₅→⁵I₈ in the UCNPs are selectively enhanced by different nanocraters. This enhancement effect is noticeable in luminescence images, as shown in Figure S7b,c (Supporting Information).

In general, the UCL enhancements are combined effects ascribed to both the increased excitation rate (absorption of the pump laser) and radiative emission rate (Purcell effect at the emission wavelength). Since the nanocraters exhibit broad spectral responses in the visible region, the enhanced radiative rates at specific emission bands rather than the enhanced excitation rate at the absorption wavelength are responsible for the observed regulation in ratiometry. This can be verified through the quantum yield analysis. The internal quantum process behind the UCL can be analyzed by calculating the internal quantum yield enhancement factor (QYEF) using the following equations^[49]

$$QYEF_{\text{green}} = \frac{QY_{(\text{crater A})}}{QY_{(\text{glass})}} = \frac{|E|_{(\text{glass})}^2 \int_{516 \text{ nm}}^{560 \text{ nm}} I_{(\text{crater A})}(\lambda) d\lambda}{|E|_{(\text{crater A})}^2 \int_{516 \text{ nm}}^{560 \text{ nm}} I_{(\text{glass})}(\lambda) d\lambda} = 2.4 \quad (1)$$

$$QYEF_{\text{red}} = \frac{QY_{(\text{crater C})}}{QY_{(\text{glass})}} = \frac{|E|_{(\text{glass})}^2 \int_{621 \text{ nm}}^{665 \text{ nm}} I_{(\text{crater C})}(\lambda) d\lambda}{|E|_{(\text{crater C})}^2 \int_{621 \text{ nm}}^{665 \text{ nm}} I_{(\text{glass})}(\lambda) d\lambda} = 1.8 \quad (2)$$

where $|E|^2$ denotes the simulated electric field at the incident light ($\lambda = 980 \text{ nm}$), $I(\lambda)$ denotes the measured UCL intensity. Indeed, the QYEF results reveal a 2.4- and 1.8-fold enhanced

radiative rate for green and red emissions by the two types of nanocraters, respectively. The increase in the radiative emission rate was confirmed by time-resolved photoluminescence (TRPL) measurement. As shown in Figure 4a,b, when deposited on the nanocraters, UCNPs showed obvious decrease in the lifetime of green (on nanocrater A) and red emission (on nanocrater C). The decreased lifetime can be ascribed to augmented Purcell factors and significantly enhanced radiative rates.

To shed light on the radiative emission rate modulation of upconversion luminescence, we performed simulation on the Purcell factor of nanocraters A and C on the MIM structure (Figure 4c,d). It should be mentioned that Purcell factors of UCNPs would vary to some extent when their locations are changed in different nanocraters since the electric field intensities vary point-by-point in these craters (Figure S8). In our study, the observed enhancement factors are mean values from a group of UCNPs self-assembled in these craters. It could be found that the obtained average Purcell factors are very close to the calculated internal quantum yield enhancements, comparable to the overall upconversion luminescence enhancement. Therefore, we can infer that the selectively augmented radiative emission rate is dominant for the regulated ratiometric upconversion emission. Notably, the R/G ratios of the UCNPs on different substrates are independent of excitation power densities, as shown in Figure S9a (Supporting Information). It can be found that the increase in the pump power results in enhanced intensities in both emission bands, while the R/G ratios exhibit negligible changes (Figure S9b–d, Supporting Information). These results suggest that the selective tuning

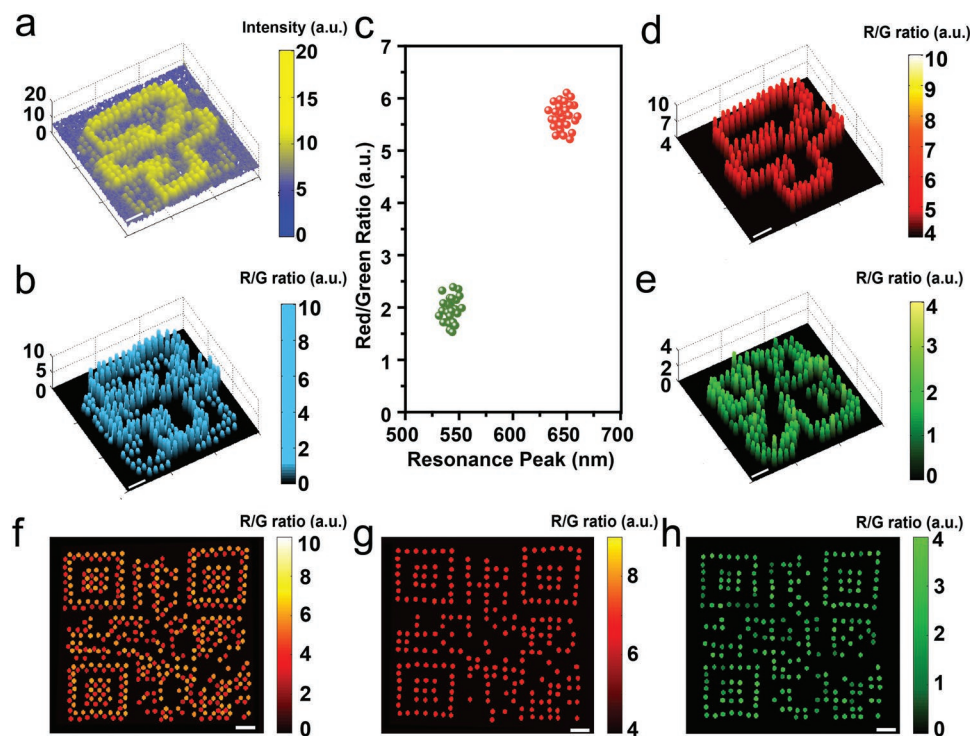


Figure 5. a) The upconversion luminescence intensity and b) R/G-ratiometric mapping of nanopattern encrypted with encoded UCNPs in the nanocraters. c) The R/G ratio of upconversion luminescence from the nanocrater patterns falls into two distributions with R/G ratios close to 1.8 and 5.5. d,e) Encrypted data can be resolved by differentiating their regulated R/G ratios. f) R/G-ratiometric mapping of QR codes encrypted with encoded UCNPs in the nanocraters. g,h) Decoding of encrypted QR codes by differentiating R/G ratios. Scale bar: 10 μm .

of the luminescence ratio is independent of the plasmon-induced thermal effect and the nonlinear nature of photon upconversion.^[43]

On the basis of controlled ratiometric emission tuning through plasmonic nanocrater printing, we further demonstrated the application of this approach for information encryption. For proof-of-concept, two sets of nanocraters with different morphologies were fabricated to form an image pattern consisting of two Chinese characters, and subsequently UCNPs solutions were spin-coated onto the pattern. It was unable to decode each encrypted character from the luminescence intensity imaging (Figure 5a). However, the two characters could be resolved by measuring the luminescence ratiometry (Figure 5b). Figure 5c indicates that the R/G ratios of the patterned structure fall into two groups with distinctly different distributions around 1.8 and 5.5. By judiciously selecting the thresholds, the encoded images could be resolved (Figure 5d,e). In addition, we demonstrated high-throughput multiple information (JNU and NUS) encryption in two binary QR codes (Figure 5f) and decryption through differentiating emission ratiometry (Figure 5g,h). Importantly, the plasmonic nanostructures can be patterned in a lithography-free fashion with large scales and fast speeds (Figure S10, Supporting Information).

In summary, we have demonstrated a ratiometric encryption strategy based on the dual-band emission modulation of a single set of UCNPs. Plasmonic nanocraters with programmable resonance peaks are fabricated through a facile laser writing technique, by which improved emission rates and luminescence enhancement at selective bands are achieved due to the

Purcell effect enabled by the splashed nanostructures. The ratiometric luminescence encryption leverages the dual-band upconversion emissions from UCNPs of fixed composition by removing the necessity of chemical synthesis of multiple sets of UCNPs of complex compositions. This technology not only offers a high-throughput method for enhancing upconversion emission but also provides a lithography-free fashion for image encryption and document security with upscalability and high spatial resolution. Moreover, this technology does not rely on any specific samples and can be extended to other UCNPs or dye-sensitized UCNPs.^[31,53] And the laser splashed nanocraters can be reproduced in large scales as plasmofluidic templates for fast biological detections^[54,55] once functional probes such as single-stranded DNA are selectively immobilized onto different craters to capture specific biological events labeled with UCNPs. We envision that our results may find potential applications in multidimensional optical data storage, information encoding, and multiplexed biological detection.

Experimental Section

Preparation of Upconversion Nanocrystals: The designed $\text{NaYF}_4:\text{Yb}/\text{Ho}/\text{Ce}@\text{NaYF}_4$ core-shell upconversion nanocrystals were synthesized by epitaxial growth mediated coprecipitation method. In a typical procedure, to a 50 mL round-bottomed flask charged with 7 mL 1-octadecene and 3 mL oleic acid was added a solution of $\text{Y}(\text{CH}_3\text{CO}_2)_3$, $\text{Yb}(\text{CH}_3\text{CO}_2)_3$, $\text{Ho}(\text{CH}_3\text{CO}_2)_3$, and $\text{Ce}(\text{CH}_3\text{CO}_2)_3$ at varied molar ratios (70/20/2/8) with a total lanthanide content of 0.4 mmol and volume of 2 mL. After heating at 150 $^\circ\text{C}$ for 1 h to remove water, the mixture

was cooled down to 50 °C, and a methanol solution containing 1.6 mmol NH₄F and 1 mmol NaOH was added. After stirring for 30 min, the mixture was heated to 100 °C and pumped for 30 min to remove methanol and possible impurities. Under an argon flow, the remaining solution was heated to 290 °C and maintained for 3 h. After cooling down, the resulting nanocrystals were washed with ethanol several times and redispersed in 4 mL of cyclohexane for succeeding shell growth. For the synthesis of NaYF₄:Yb/Ho/Ce@NaYF₄ core-shell upconversion nanocrystals, a shell precursor containing 0.4 mmol Y(CH₃CO₂)₃ was prepared and kept at 80 °C. Then as-synthesized NaYF₄:Yb/Ho/Ce core nanocrystals were added in the shell precursor. After 30 min, upon the removal of excess cyclohexane, the resultant mixture was cooled down to 50 °C and a 6 mL methanol solution of NH₄F and NaOH was added. After stirring for another 30 min, the reaction was kept at 100 °C and pumped for 15 min before reaching 290 °C. After reaction for 2 h in argon, the prepared core-shell nanocrystals were washed with ethanol and redispersed cyclohexane for further use.

Fabrication of Plasmonic Nanocraters: The sample was mounted to a 3D translation stage that was controlled by the computer (Figure S11, Supporting Information). The femtosecond pulsed laser beam (40 fs at 800 nm) was focused onto the sample after a tunable attenuator. Then the reflected light from the sample was collected by a charge coupled device (CCD) to monitor the fabrication. The laser pulse and the piezo stage are coordinately controlled by the computer to realize printing of arbitrary patterns.

Numerical Simulations: Simulations of the scattering spectra were carried out using FDTD methods (Lumerical FDTD Solutions). The complex refractive indices of silicon, silver, and titanium were taken from Palik,^[56] and the index of silicon nitride was set as 2.05. Perfectly matched layers (PML) boundary conditions were defined around the nanostructure at a minimum of half a wavelength away. A total field/scattered-field source was launched incident to the nanostructure, and the scattering power was collected by evaluating the near-to-far-field projection over a cone defined by the NA of the objective lens. Electric field distribution cross-section is detected by a 2D field profile monitor in the *x-z* plane.

Characterization of the UCL and TRPL: The UCL spectra of the samples were collected by a spectrometer (Shamrock 303i, Andor) upon irradiation at 980 nm. Emission lifetime measurements of UCNPs were performed by modulating the 980 nm laser with a chopper (model SR540, Stanford). The triggered signal from the chopper was synchronized with a time-correlated single-photon counter (NanoHarp, Picoquant) to record the emission photons.

Supporting Information

Supporting Information is available from the Wiley Online Library or from the author.

Acknowledgements

Z.F., D.H., and L.L. contributed equally to this work. This research was supported by National Key R&D Program of China (YS2018YFB110012), National Natural Science Foundation of China (NSFC) (Grant No. 61522504 and 21317137), Guangdong Provincial Innovation and Entrepreneurship Project (Grant No. 2016ZT06D081), the Singapore Ministry of Education (MOE2017-T2-2-110), and Agency for Science, Technology and Research (A*STAR) (Grant No. A1883c0011). The authors would like to thank Prof. Yaohua Mai (Jinan University) for providing the access to the SEM facilities.

Conflict of Interest

The authors declare no conflict of interest.

Keywords

laser splashing, plasmonic nanocrater, ratiometric encryption, upconversion nanoparticles

Received: April 13, 2019

Revised: June 1, 2019

Published online:

- [1] P. Zijlstra, J. W. Chon, M. Gu, *Nature* **2009**, 459, 410.
- [2] X. Li, T. H. Lan, C. H. Tien, M. Gu, *Nat. Commun.* **2012**, 3, 998.
- [3] Z. L. Deng, J. Deng, X. Zhuang, S. Wang, K. Li, Y. Wang, Y. Chi, X. Ye, J. Xu, G. P. Wang, *Nano Lett.* **2018**, 18, 2885.
- [4] H. Dong, L. D. Sun, W. Feng, Y. Gu, F. Li, C. H. Yan, *ACS Nano* **2017**, 11, 3289.
- [5] H. Yun, S. Y. Lee, K. Hong, J. Yeom, B. Lee, *Nat. Commun.* **2015**, 6, 7133.
- [6] Y. Zhang, L. Zhang, R. Deng, J. Tian, Y. Zong, D. Jin, X. Liu, *J. Am. Chem. Soc.* **2014**, 136, 4893.
- [7] F. Walter, G. Li, C. Meier, S. Zhang, T. Zentgraf, *Nano Lett.* **2017**, 17, 3171.
- [8] S. M. Kamali, E. Arbabi, A. Arbabi, Y. Horie, M. Faraji-Dana, A. Faraon, *Phys. Rev. X* **2017**, 7, 041056.
- [9] D. Hu, Y. Lu, Y. Cao, Y. Zhang, Y. Xu, W. Li, F. Gao, B. Cai, B.-O. Guan, C.-W. Qiu, *ACS Nano* **2018**, 12, 9233.
- [10] H. Ren, X. Li, Q. Zhang, M. Gu, *Science* **2016**, 352, 805.
- [11] Y. Li, X. Li, L. Chen, M. Pu, J. Jin, M. Hong, X. Luo, *Adv. Opt. Mater.* **2017**, 5, 1600502.
- [12] G. Gibson, J. Courtial, M. J. Padgett, M. Vasnetsov, V. Pas'ko, S. M. Barnett, S. Franke-Arnold, *Opt. Express* **2004**, 12, 5448.
- [13] K. Jiang, L. Zhang, J. Lu, C. Xu, C. Cai, H. Lin, *Angew. Chem., Int. Ed.* **2016**, 55, 7231.
- [14] B. Hardwick, W. Jackson, G. Wilson, A. W. Mau, *Adv. Mater.* **2001**, 13, 980.
- [15] F. Zhang, Q. Shi, Y. Zhang, Y. Shi, K. Ding, D. Zhao, G. D. Stucky, *Adv. Mater.* **2011**, 23, 3775.
- [16] Y. Li, Y. T. Cu, D. Luo, *Nat. Biotechnol.* **2005**, 23, 885.
- [17] X. Hou, C. Ke, C. J. Bruns, P. R. McGonigal, R. B. Pettman, J. F. Stoddart, *Nat. Commun.* **2015**, 6, 6884.
- [18] R. Deng, F. Qin, R. Chen, W. Huang, M. Hong, X. Liu, *Nat. Nanotechnol.* **2015**, 10, 237.
- [19] F. Wang, Y. Han, C. S. Lim, Y. Lu, J. Wang, J. Xu, H. Chen, C. Zhang, M. Hong, X. Liu, *Nature* **2010**, 463, 1061.
- [20] Q. Zhan, H. Liu, B. Wang, Q. Wu, R. Pu, C. Zhou, B. Huang, X. Peng, H. Agren, S. He, *Nat. Commun.* **2017**, 8, 1058.
- [21] X. Zhu, J. Li, X. Qiu, Y. Liu, W. Feng, F. Li, *Nat. Commun.* **2018**, 9, 2176.
- [22] L. Liang, X. Xie, D. T. Loong, A. H. All, L. Huang, X. Liu, *Chem. - Eur. J.* **2016**, 22, 10801.
- [23] M. He, X. Pang, X. Liu, B. Jiang, Y. He, H. Snaith, Z. Lin, *Anal. Chem.* **2016**, 128, 4352.
- [24] X. Huang, S. Han, W. Huang, X. Liu, *Chem. Soc. Rev.* **2013**, 42, 173.
- [25] L. Liang, Y. Liu, C. Bu, K. Guo, W. Sun, N. Huang, T. Peng, B. Sebo, M. Pan, W. Liu, *Adv. Mater.* **2013**, 25, 2174.
- [26] X. Chen, L. Jin, W. Kong, T. Sun, W. Zhang, X. Liu, J. Fan, S. F. Yu, F. Wang, *Nat. Commun.* **2016**, 7, 10304.
- [27] A. Fernandez-Bravo, K. Yao, E. S. Barnard, N. J. Borys, E. S. Levy, B. Tian, C. A. Tajon, L. Moretti, M. V. Altoe, S. Aloni, *Nat. Nanotechnol.* **2018**, 1.
- [28] J. Zhao, D. Jin, E. P. Schartner, Y. Lu, Y. Liu, A. V. Zvyagin, L. Zhang, J. M. Dawes, P. Xi, J. A. Piper, *Nat. Nanotechnol.* **2013**, 8, 729.
- [29] M. You, M. Lin, S. Wang, X. Wang, G. Zhang, Y. Hong, Y. Dong, G. Jin, F. Xu, *Nanoscale* **2016**, 8, 10096.

- [30] M. You, J. Zhong, Y. Hong, Z. Duan, M. Lin, F. Xu, *Nanoscale* **2015**, 7, 4423.
- [31] X. Wu, Y. Zhang, K. Takle, O. Bilsel, Z. Li, H. Lee, Z. Zhang, D. Li, W. Fan, C. Duan, *ACS Nano* **2016**, 10, 1060.
- [32] S. Wu, N. Duan, Z. Shi, C. Fang, Z. Wang, *Anal. Chem.* **2014**, 86, 3100.
- [33] L. Liang, X. Qin, K. Zheng, X. Liu, *Acc. Chem. Res.* **2019**, 52, 228.
- [34] Y. Lu, J. Lu, J. Zhao, J. Cusido, F. M. Raymo, J. Yuan, S. Yang, R. C. Leif, Y. Huo, J. A. Piper, J. P. Robinson, E. M. Goldys, D. Jin, *Nat. Commun.* **2014**, 5, 3741.
- [35] Y. Lu, J. Zhao, R. Zhang, Y. Liu, D. Liu, E. M. Goldys, X. Yang, P. Xi, A. Sunna, J. Lu, Y. Shi, R. C. Leif, Y. Huo, J. Shen, J. A. Piper, J. P. Robinson, D. Jin, *Nat. Photonics* **2014**, 8, 32.
- [36] R. Deng, X. Liu, *Nat. Photonics* **2014**, 8, 10.
- [37] H. Liu, M. K. Jayakumar, K. Huang, Z. Wang, X. Zheng, H. Agren, Y. Zhang, *Nanoscale* **2017**, 9, 1676.
- [38] M. Saboktakin, X. Ye, S. J. Oh, S.-H. Hong, A. T. Fafarman, U. K. Chettiar, N. Engheta, C. B. Murray, C. R. Kagan, *ACS Nano* **2012**, 6, 8758.
- [39] W. Zhang, F. Ding, S. Y. Chou, *Adv. Mater.* **2012**, 24, OP236.
- [40] Z. Yin, D. Zhou, W. Xu, S. Cui, X. Chen, H. Wang, S. Xu, H. Song, *ACS Appl. Mater. Interfaces* **2016**, 8, 11667.
- [41] F. Kang, J. He, T. Sun, Z. Y. Bao, F. Wang, D. Y. Lei, *Adv. Funct. Mater.* **2017**, 27, 1701842.
- [42] M. Saboktakin, X. Ye, U. K. Chettiar, N. Engheta, C. B. Murray, C. R. Kagan, *ACS Nano* **2013**, 7, 7186.
- [43] W. Zhang, J. Li, H. Lei, B. Li, *ACS Appl. Mater. Interfaces* **2017**, 9, 42935.
- [44] Q. Zhan, X. Zhang, Y. Zhao, J. Liu, S. He, *Laser Photonics Rev.* **2015**, 9, 479.
- [45] E. Verhagen, L. Kuipers, A. Polman, *Opt. Express* **2009**, 17, 14586.
- [46] J. Tong, F. Suo, J. Ma, L. Y. Tobing, L. Qian, D. H. Zhang, *Opto-Electron. Adv.* **2018**, 2, 180026.
- [47] A. L. Feng, M. L. You, L. Tian, S. Singamaneni, M. Liu, Z. Duan, T. J. Lu, F. Xu, M. Lin, *Sci. Rep.* **2015**, 5, 7779.
- [48] A. L. Feng, M. Lin, L. Tian, H. Y. Zhu, H. Guo, S. Singamaneni, Z. Duan, T. J. Lu, F. Xu, *RSC Adv.* **2015**, 5, 76825.
- [49] K. Park, K. Jung, S. J. Kwon, H. S. Jang, D. Byun, I. K. Han, H. Ko, *Adv. Funct. Mater.* **2016**, 26, 7836.
- [50] K. Park, M. Park, H. S. Jang, J. H. Park, J. Kim, Y. Cho, I. K. Han, D. Byun, H. Ko, *Adv. Funct. Mater.* **2018**, 28, 1800369.
- [51] S. Han, R. Deng, X. Xie, X. Liu, *Angew. Chem., Int. Ed.* **2014**, 53, 11702.
- [52] E. Dulkeith, A. Morteani, T. Niedereichholz, T. Klar, J. Feldmann, S. Levi, F. Van Veggel, D. Reinhoudt, M. Möller, D. Gittins, *Phys. Rev. Lett.* **2002**, 89, 203002.
- [53] X. Wu, H. Lee, O. Bilsel, Y. Zhang, Z. Li, T. Chen, Y. Liu, C. Duan, J. Shen, A. Punjabi, *Nanoscale* **2015**, 7, 18424.
- [54] X. Peng, B. B. Rajeeva, D. Teal, Y. Zheng, *Nanotechnology Characterization Tools for Biosensing and Medical Diagnosis*, Springer, Berlin **2018**, p. 213.
- [55] P. P. Patra, R. Chikkaraddy, R. P. Tripathi, A. Dasgupta, G. P. Kumar, *Nat. Commun.* **2014**, 5, 4357.
- [56] E. D. Palik, *Handbook of Optical Constants of Solids*, Academic, San Diego, CA **1998**.